

Bayesian model-scenario averaged predictions of compressor cascade flows under uncertain turbulence models

M. de Zordo-Banliat^{a,b}, X. Merle^b, G. Dergham^a, P. Cinnella^b

^a Safran Tech, Modelling & Simulation, Rue des Jeunes Bois, Châteaufort, 78114 Magny-Les-Hameaux, France

^b DynFluid Laboratory - Arts et Métiers ParisTech - 151 boulevard de l'Hôpital, 75013 Paris, France

Abstract

The Reynolds-Averaged Navier-Stokes (RANS) equations represent the computational workhorse for engineering design, despite their numerous flaws. Improving and quantifying the uncertainties associated with RANS models is particularly critical in view of the analysis and optimization of complex turbomachinery flows. In this work, we use Bayesian inference for assimilating data into RANS models for the following purposes: (i) updating the model closure coefficients for a class of turbomachinery flows, namely a compressor cascade; (ii) quantifying the parametric uncertainty associated with closure coefficients of RANS models and (iii) quantifying the uncertainty associated with the model structure and the choice of the calibration dataset based on an ensemble of concurrent models and calibration scenarios. Inference of the coefficients of three widely employed RANS models is carried out from high-fidelity LES data for the NACA65 V103 compressor cascade [1, 2]. Posterior probability distributions of the model coefficients are collected for various calibration scenarios, corresponding to different values of the flow angle at inlet. The Maximum A Posteriori estimates of the coefficients differ from the nominal values and depend on the scenario. A recently proposed Bayesian mixture approach, namely, Bayesian Model-Scenario Averaging (BMSA) [3, 4], is used to build a prediction model that takes into account uncertainties associated with alternative model forms and with sensitivity to the calibration scenario. Stochastic predictions are presented for the turbulent flow around the NACA65 V103 cascade at mildly and severe off-design conditions. The results show that BMSA generally yields more accurate solutions than the baseline RANS models and succeeds well in providing an estimate for the predictive uncertainty intervals, provided that a sufficient diversity of scenarios and models is included in the mixture.

Keywords: Compressor Flow, RANS Models, Bayesian Model Averaging, Uncertainty Quantification.

1. Introduction

1 The design of modern, highly-loaded axial compres-
2 sors requires accurate predictions of stagnation pressure
3 losses at the early stages of the design process. Com-
4 pressor flows are characterized by high relative speeds,
5 leading to the formation of shock waves interacting
6

Email addresses:

maximilien.de-zordo-banliat@safrangroup.com (M. de
Zordo-Banliat), merle.xavier@ensam.eu (X. Merle),
gregory.dergham@safrangroup.com (G. Dergham),
paola.cinnella@ensam.eu (P. Cinnella)

Preprint submitted to Elsevier

October 22, 2019

7 with the surrounding boundary layers, as well as by the
8 development of secondary flows (such as corner and
9 tip vortices) at blade roots and tips, which interact with
10 the hub and casing and have a strong impact on flow
11 development and on the resulting efficiencies. Addi-
12 tional complexity is introduced by laminar-to-turbulent
13 flow transition induced by high-intensity incoming
14 freestream turbulence (bypass transition) or by flow
15 separation under strongly adverse pressure gradients,
16 for example.

17
18 Although flawed by numerous major deficiencies
19 –especially for strongly non-equilibrium and pos-
20 sibly transitional flows like those of interest here–,
21 Reynolds-Averaged Navier–Stokes (RANS) modelling
22 remains the workhorse for turbomachinery design. The
23 main reason is that, despite considerable advances of
24 so-called high-fidelity simulations (namely, Direct Nu-
25 merical Simulation, DNS, and Large Eddy Simulation,
26 LES) in terms of applicability to more geometrically
27 complex configurations and to higher Reynolds number
28 flows (including turbomachinery flows, see [5]), the
29 computational cost of such simulations remains hun-
30 dreds of times higher than RANS.

31
32 RANS modelling uncertainties can be classified into
33 four levels [6]: 1) uncertainties related to the validity
34 of the averaging process itself; 2) uncertainties in rep-
35 resenting the unclosed Reynolds stress tensor as a func-
36 tion of the mean field; 3) uncertainties in the constitu-
37 tive law used to relate the Reynolds stresses to the mean
38 field; 4) uncertainties in the closure parameters associ-
39 ated with a given model form. A review of turbulence
40 modelling uncertainties and of methodologies for quan-
41 tifying and reducing such uncertainties can be found in

42 [7]. Several authors have recently investigated the pos-
43 sibility of using high-fidelity simulation data for devel-
44 oping improved RANS models for restricted classes of
45 flows (see [6] for a review). For instance, in [8] the
46 source terms of the Spalart–Allmaras were learnt from
47 data using a single hidden layer neural network, which
48 served as a first feasibility study. In [9], a multiplica-
49 tive correction function was introduced in the turbulent
50 kinetic energy production term of the k -equation for the
51 $k-\omega$ model. The correction was determined via inverse
52 modelling and served to train a Gaussian process. In
53 [10], a deep neural network was trained to predict the
54 anisotropic part of the Reynolds stress tensor. The net-
55 work was designed to embed Galilean invariance of the
56 predicted stresses. The above-mentioned data-driven
57 methods all try to develop corrections of some under-
58 lying RANS model, in particular by relaxing the well-
59 known “Boussinesq approximation” or “linear eddy vis-
60 cosity” hypothesis, which is the keystone of a large ma-
61 jority of RANS models used in industrial applications.
62 A particularly promising data-driven approach has been
63 introduced in [11], based on Gene-Expression Program-
64 ming (GEP). Such an approach leads to the develop-
65 ment of Explicit Algebraic Stress Models (EARSMS), a
66 class of RANS models using nonlinear constitutive rela-
67 tions for the Reynolds stresses [12], directly from high-
68 fidelity data. These models relax the linear eddy viscos-
69 ity hypothesis, leading to improved and yet computa-
70 tionally cheap (compared to high-fidelity) RANS mod-
71 els. The GEP approach has been recently used to de-
72 velop tailor-made EARSMS for turbine flows [13]. An
73 alternative approach for EARSMS discovery, based on
74 sparse deterministic regression, has been recently pro-
75 posed in [14].

76 GEP, as well as other of the above-mentioned

77 data-driven methods, belong to the class of "non para- 112
78 metric" [7] methods for quantifying RANS modelling 113
79 inadequacy, which try to formulate a correction to the 114
80 model form (most often, the constitutive law for the 115
81 Reynolds stress tensor) based on the observed data. 116
82 Such non parametric methods have recently attracted 117
83 considerable interest from the scientific community 118
84 due to their potential for automatic learning of RANS 119
85 models from data, but suffer from the following 120
86 limitations: 1) they tend to lack generality, *i.e.*, they 121
87 work well for flows similar to those in the training 122
88 set but can be hardly extrapolated to different flows; 123
89 2) they need a significant amount of high-fidelity 124
90 data (generally costly to obtain and limited to simple, 125
91 low-Reynolds number configurations) and are not well 126
92 suited for incomplete, noisy data such as experiments; 127
93 3) in most cases, they lead to deterministic predictions 128
94 and do not provide estimates of confidence intervals 129
95 due to persisting uncertainties in both model form and 130
96 closure coefficients. For turbomachinery design (and 131
97 for engineering design in general), confidence intervals 132
98 on the predicted quantities of interest (QoI) represent as 133
99 valuable information as the QoI itself, since they allow 134
100 estimating uncertainties about the expected system 135
101 performance early in the design phase. This is why, in 136
102 this work, we focus instead on "parametric" uncertainty 137
103 quantification approaches [7]. The latter use some 138
104 available data for estimating and reducing uncertainties 139
105 in model closure coefficients, given the model form. 140
106 A natural framework for parametric approaches is 141
107 Bayesian inference, whereby the model coefficients 142
108 are assigned *a priori* probability distributions (based, 143
109 *e.g.*, on literature data or expert judgement) that are 144
110 *a posteriori* updated by using data. Since the model 145
111 coefficients are now represented as probability distri- 146

112 butions, the model output is also a random quantity,
113 characterized by a probability distribution. In other
114 terms, the solution is naturally equipped with uncer-
115 tainty intervals. Parametric approaches can be easily
116 applied to small, noisy datasets and can be successively
117 updated as soon as new or better data become available.
118 Refs [15, 3] used Bayesian inference for calibrating the
119 Spalart–Allmaras and $k - \varepsilon$ models, respectively, by us-
120 ing experimental data for turbulent flat plate boundary
121 layers. Although parametric approaches only infer on
122 model coefficients, they can also be used for estimating,
123 to some extent, model-form uncertainties. One way to
124 do that is to adopt multi-model ensemble techniques,
125 which have been used in a variety of applications,
126 including aerodynamics [16, 17, 18, 19, 20, 21]. Here
127 we focus on the Bayesian Model Averaging (BMA)
128 framework, initially proposed by Draper [22] (see also
129 [23]). A significant extension to BMA is represented
130 by Bayesian Model-Scenario Averaging (BMSA)
131 [21, 3, 4]. Like BMA, BMSA combines the predictions
132 from multiple models, thereby providing a measure
133 for model uncertainty, using posterior distributions
134 of the coefficients inferred from different calibration
135 scenarios. In [3], a BMSA model was constructed
136 by averaging five RANS models calibrated on 14
137 scenarios, corresponding to turbulent flat plate flows
138 subject to various external pressure gradients. BMSA,
139 calibrated on the scenarios of [3], was successfully
140 applied to a transonic wing configuration in [4].

In the present work we investigate the potential of BMSA for robust predictions of turbomachinery flows under uncertain RANS models, with focus on a compressor cascade. We focus more particularly on the NACA65 V103 compressor cascade, for which high-

147 fidelity numerical and experimental data are available
 148 in the literature. For our study, we select three widely
 149 used RANS models, namely, the Spalart–Allmaras [24],
 150 Wilcox’ $k - \omega$ [25], and Launder–Sharma $k - \varepsilon$ [26] tur-
 151 bulence models. The purpose of the study is manifold:
 152 1) we investigate if BMSA calibrated on elementary ex-
 153 ternal flow configurations like those of [3, 4] may still
 154 provide valuable information for the internal flow con-
 155 figuration of interest; 2) we set up a computationally
 156 efficient strategy for specifically calibrating BMSA for
 157 costly compressor flows; 3) finally, we apply BMSA to
 158 the NACA65 V103 compressor flow at operating condi-
 159 tions outside the calibration set, and we assess its capa-
 160 bility to provide accurate predictions and the associated
 161 uncertainty intervals for new flows. The results are com-
 162 pared to those of BMSA based on the on-the-shelf sets
 163 of coefficients [4].

164 The paper is organized as follows. In Section 2, we
 165 recall the Bayesian framework, with special focus on
 166 BMSA. In Section 3, we describe the compressor flow
 167 configuration and the RANS models. In Section 4 we
 168 report BMSA results for the NACA65 V103 cascade at
 169 two off-design conditions. Finally, Section 5 summa-
 170 rizes the main findings and draws perspectives for future
 171 work.

172 2. Bayesian framework

173 In this section, we recall the theoretical framework
 174 for Bayesian model calibration and BMSA, following
 175 [27].

176 2.1. Bayesian calibration

Let us consider a physical model of the form:

$$\Delta = M(\theta) \quad (1)$$

177 with $\Delta = (\Delta_1, \dots, \Delta_N)$ a vector of Quantities of Interest
 178 (QoI) computed by a model M given a set of parameters
 179 θ of dimension P .

180 In the deterministic framework, the components of
 181 θ are perfectly known and have a fixed value. In the
 182 Bayesian framework, the unknown parameters vector θ
 183 is treated as a random vector, characterised by a joint
 184 probability density function (pdf), noted f . Due to the
 185 uncertainty on θ , Δ is also a random vector.

The scope of Bayesian inference is to gain new
 knowledge about θ by constructing an improved repre-
 sentation of its pdf, based on prior knowledge and as-
 similating the observed data. For that purpose, let us
 note D the random vector of observed high-fidelity data.
 Bayes rules states that :

$$f(\theta|D = \bar{D}) = \frac{f(D = \bar{D}|\theta)}{f(D = \bar{D})} f(\theta) \quad (2)$$

186 Here, $f(\theta)$ is the prior pdf and represents the initial be-
 187 lief about θ , $f(D = \bar{D}|\theta)$ is the likelihood and corre-
 188 sponds to the probability to observe \bar{D} , a realisation of
 189 the random variable D , if θ is known exactly. The pos-
 190 terior pdf $f(\theta|D = \bar{D})$ represents the updated knowledge
 191 of θ given the observed data vector \bar{D} , of size N . In prac-
 192 tice, calibration compares the model prediction and the
 193 observations to extract the pdf of the parameters vector
 194 θ that is the most likely to capture the data. In our case,
 195 θ is the set of closure parameters associated with a given
 196 RANS model.

197 From Eq. (2), it appears that the posterior distribution
 198 is entirely determined by the prior and likelihood func-
 199 tion. Following Arnst [28] we use uninformative priors,
 200 *i.e.* uniform priors, for each component of θ (supposed
 201 independent). As RANS models have been carefully de-
 202 signed, we are confident in assuming that the standard
 203 values should be included in the range of the prior. We

204 therefore choose uniform priors that include standard 229
 205 values (reported in Table 2), as done in [15] [3]. Further- 230
 206 more, there is no evidence that model predictions would 231
 207 be improved by choosing closure coefficients with sig- 232
 208 nificant deviations from the standard values. The prior 233
 209 intervals are therefore chosen to be large enough to al- 234
 210 low a good exploration of the parameter space, while 235
 211 avoiding values preventing the CFD solver to converge. 236
 212 Also note that excessively large prior distributions may 237
 213 lead to overfitting problems, resulting in posterior coef- 238
 214 ficients that fit very well the calibration data, but deteri- 239
 215 orate predictions of unobserved quantities of interest.

216 The likelihood function $f(D = \bar{D}|\theta)$ is a statistical
 217 model for observation errors (discrepancies between the
 218 data and their true, unobserved, values) and model in-
 219 adequacies. The latter accounts for the fact that part of
 220 the physics is missed by the model due to any approx-
 221 imation introduced in its construction, so that the true
 222 phenomenon can never be exactly captured, even with
 223 the best possible model coefficients.

In the present calculations, the observation error is
 modelled as an additive noise and the model inadequacy
 as a multiplicative term, as also done in [15]. Specifi-
 cally, the data \bar{D} at a given location x_i are related to the
 observation error by:

$$\bar{D}(x_i) = \widehat{D}(x_i) + e_i(x_i) \quad (3)$$

224 with e_i the observation noise at position x_i and $\widehat{D}(x_i)$ the
 225 (unobserved) true value of the QoI vector. We choose
 226 the components of the observation noise to be indepen-
 227 dent and normally distributed, with zero mean and a
 228 standard deviation equal to 1% of the observed value.

The model-inadequacy η_i is given by:

$$\widehat{D}(x_i) = \eta_i \Delta(x_i, \theta) \quad (4)$$

with $\Delta(x_i, \theta)$ the model output at a point x_i . We choose
 the model errors to be independent and Gaussian, *i.e.*
 $\eta_i \sim \mathcal{N}(1, \sigma_\eta^2)$ where σ_η is an additional uncertain
 hyper-parameter that needs to be calibrated, and there-
 fore is concatenated to the vector of parameters θ . The
 hyperparameter σ_η is a measure of the magnitude of the
 model inadequacy and thus can be taken as an indica-
 tor of the accuracy of a given model, calibrated for a
 given scenario. Considering a model error mitigates the
 influence of overfitting on the calibration, as it relaxes
 constraints. For more detailed discussion, see [22].

The preceding choices for η_i and e_i lead to a likeli-
 hood function of the form:

$$f(\bar{D}|\Delta, \theta) = \frac{1}{\sqrt{(2\pi)^N |K|}} \exp \left[-\frac{1}{2} (\bar{D} - \Delta(\theta))^T K^{-1} (\bar{D} - \Delta(\theta)) \right] \quad (5)$$

with $K = K_e + K_M$ where K_e is a diagonal matrix repre-
 senting the observational error vector and $K_M = \sigma_\eta^2 I$ a
 diagonal matrix reflecting model inadequacy.

For complex models like those of interest in this
 study, the term $\Delta(\theta)$ cannot be computed analytically,
 and the posterior distribution for θ must be approx-
 imated numerically. Specifically, we use a Markov-
 Chain Monte-Carlo method to draw sample from the
 posterior pdf, and namely the Metropolis-Hastings al-
 gorithm [29] available in the *pymc*¹ open library. The
 MCMC sampling is stopped when the following crite-
 ria are satisfied: the Geweke z-score [30], the steady-
 ness of the first two moments of the sample, and the
 auto-correlation of the Markov Chain. For more details
 concerning such creteria, we refer to [27].

Typically, $\mathcal{O}(10^5)$ samples are needed to reach con-
 vergence, which is unacceptably high for costly RANS
 models. To reduce the computational effort to an

¹<https://github.com/pymc-devs/pymc>

258 amenable level, the calibrations presented in the follow-
 259 ing are based on surrogate models, presented in section
 260 3.4.

261 2.2. BMSA formulation

262 In this paper we call scenario, noted S , a specific flow
 263 case unambiguously described by a known and deter-
 264 ministic set of parameters (e.g. the geometry of the
 265 blade, boundary conditions, Reynolds Number, Mach
 266 number...). Now, consider $i = 1, \dots, I$ models applica-
 267 ble to a set of $k = 1, \dots, K$ scenarios $\mathcal{S} = \{S_1, \dots, S_K\}$
 268 for which we have K vectors of observed data $\mathcal{D} =$
 269 $\{\overline{D}_1, \dots, \overline{D}_K\}$. Similarly, we call $\mathcal{M} = \{M_1, \dots, M_I\}$ the
 270 ensemble of all available models. For each model ap-
 271 plied to each scenario, we assume that the calibration
 272 phase resulted in a posterior for θ , *i.e.*

$$\theta_{i,k} \sim \theta | M = M_i, S = S_k, D = \overline{D}_k \quad (6)$$

Aftwards, let us consider a new scenario S' with no
 available data and a QoI Δ . Similarly to [22], we use
 the law of total probabilities to state that :

$$f(\Delta | S', \mathcal{D}, \mathcal{M}, S) = \sum_{i=1}^I \sum_{k=1}^K f(\Delta | S', \overline{D}_k, M_i, S_k) p(M_i | \overline{D}_k, S_k) p(S_k) \quad (7)$$

273 Here, $f(\Delta | S', D = \overline{D}_k, M = M_i, S = S_k)$ represents
 274 the distribution of Δ obtained by propagating the pos-
 275 terior distribution $\theta_{i,k}$ for the new scenario S' , p is the
 276 probability mass function of a discrete random variable
 277 and we assumed that D and S are independent, as in
 278 [21]. For the sake of conciseness, we drop the clearer
 279 but redundant formulation $M = M_i$ or $S = S_k$ to simply
 280 write M_i or S_k in the rest of the paper. We also deliber-
 281 ately omit \mathcal{D} , \mathcal{M} and S in $f(\Delta | S')$ for the same reason.

Equation (7) leads to the following expression for the
 two leading moments of $f(\Delta | S')$:

$$E[\Delta | S'] = \sum_{i=1}^I \sum_{k=1}^K E[\Delta | S', \overline{D}_k, M_i, S_k] p(M_i | \overline{D}_k, S_k) p(S_k) \quad (8)$$

$$\begin{aligned} Var[\Delta | S'] = & \sum_{i=1}^I \sum_{k=1}^K Var[\Delta | S', \overline{D}_k, M_i, S_k] \\ & \underbrace{p(M_i | \overline{D}_k, S_k) p(S_k)}_{\text{within-model, within-scenario variance}} \\ & + \sum_{i=1}^I \sum_{k=1}^K \underbrace{\left(E[\Delta | S', \overline{D}_k, M_i, S_k] - E[\Delta | S', \overline{D}_k, \mathcal{M}, S_k] \right)^2}_{p(M_i | \overline{D}_k, S_k) p(S_k)} \\ & \underbrace{\quad}_{\text{between-model, within-scenario variance}} \\ & + \sum_{k=1}^K \underbrace{\left(E[\Delta | S', \overline{D}_k, \mathcal{M}, S_k] - E[\Delta | S', \mathcal{Z}, \mathcal{M}, S_k] \right)^2}_{p(S_k)} \\ & \underbrace{\quad}_{\text{between-scenario variance}} \end{aligned} \quad (9)$$

In Eq. (9) the variance $Var[\Delta | S']$ is decomposed
 in three contributions: the first one is related to the
 parametric uncertainty and accounts for the dispersion
 within the samples $\theta_{i,k}$. As such samples have been
 obtained in the calibration phase for given model and
 scenario, this first term is called *within-model, within-*
scenario variance. The second term represents variance
between model, within scenario and grows when mod-
 els give contradicting predictions for the same scenario.
 The final term, called *between scenario variance*, re-
 flects the fact that using different calibration scenario re-
 sults in different posteriors for $\theta_{i,k}$ and in different model
 probabilities $p(M_i | \overline{D}_k, S_k)$. This ultimately leads to dif-
 ferent predictions for $\Delta | S'$.

The term

$$E[\Delta | S', \overline{D}_k, \mathcal{M}, S_k]$$

in Eqs (8) and (9) represents the mean of Δ averaged

over all the models being calibrated on the same scenario. It is computed through :

$$E \left[\Delta | S', \overline{D}_k, \mathcal{M}, S_k \right] = \sum_{i=1}^I E \left[\Delta | S', \overline{D}_k, M_i, S_k \right] p(M_i | \overline{D}_k, S_k) p(S_k) \quad (10)$$

The posterior model probability $p(M_i, S_k | \overline{D}_k)$ reflects how well the model M_i fits the data \overline{D}_k for the scenario S_k . It can be computed through the Bayes rule:

$$p(M_i | \overline{D}_k, S_k) = \frac{p(\overline{D}_k | M_i, S_k) p(M_i | S_k)}{\sum_{j=1}^J p(\overline{D}_k | M_j, S_k) p(M_j | S_k)} \quad (11)$$

where $p(M_i | S_k)$ is a user-defined prior and $p(\overline{D}_k | M_i, S_k)$ is the model evidence :

$$p(\overline{D}_k | M_i, S_k) = \int_{\Theta} f(\overline{D}_k | \theta, M_i, S_k) f(\theta | M_i, S_k) d\theta \quad (12)$$

$p(M_i | S_k)$ is generally chosen equiproportional, i.e.

$$p(M_i | S_k) = 1/I.$$

The BMSA formulation is completed by selecting a prior probability mass function for the scenarios, i.e. an expression for $p(S_k)$. It was shown in [3] that choosing a uniform prior for the scenario mass function brings unnecessary large variance. Following [4] and [27], we choose prior scenario based on model agreement:

$$\begin{cases} p(S = S_k) = \frac{\varepsilon_k^{-p}}{\sum_{k=1}^K \varepsilon_k^{-p}} \\ \varepsilon_k = \sum_{i=1}^I \left\| E \left[\Delta | S', \overline{D}_k, M_i, S_k \right] - E \left[\Delta | S', \overline{D}_k, \mathcal{M}, S_k \right] \right\|_2 \end{cases} \quad (13)$$

with $p = 2$. In this formulation, scenarios for which models give closer predictions are assigned higher probabilities.

3. Case Setup and Methodology

3.1. Compressor cascade configuration and reference data

In the following, BMSA is used to predict a compressor flow configuration. Specifically, we focus on the

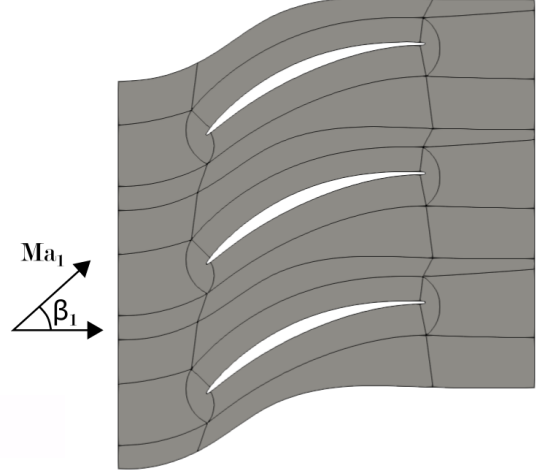


Figure 1: Sketch of the compressor Cascade V 103 adapted from [32]. Ma_1 is the inlet Mach and β_1 is the angle of attack.

NACA65 V103 cascade from Leipold [31], sketched in Figure 1, which is representative of a realistic axial compressor mid-section. For this cascade, the design conditions correspond to an inlet flow angle $\beta_1 = 42^\circ$, an inlet Mach number of 0.67 and a Reynolds number (based on the blade axial chord and the inlet quantities) equal to 450000, respectively. This configuration has been widely studied in the past years [32, 33, 1], and the high-fidelity data available in the literature are suitable for BMSA calibration and assessment. Hereafter we consider in particular the LES data from Leggett [1, 2], who investigated the cascade at four off-design conditions, corresponding to calibration/prediction scenarios in the present Bayesian framework. The scenarios have different values of inlet angle but similar inlet Reynolds and Mach numbers and inlet turbulence intensities. Flow conditions characterizing each scenario are reported in Table 1. Previous study [1] pointed out that RANS models provide rather accurate results for near design conditions, but behave poorly at off-design.

| Scenario | S_1 | S_2 | S_3 | S_4 |
|-----------|--------|--------|--------|-------|
| β_1 | 36.99° | 39.97° | 44.09° | 49.2° |
| Ma_1 | 0.654 | 0.674 | 0.666 | 0.65 |
| Re_1 | 302K | 302K | 298K | 289K |
| Tu (%) | 2.9 | 3.4 | 3.4 | 3.5 |

Table 1: Flow conditions for various compressor cascade scenarios.

The NACA 65 V103 cascade therefore represents a challenging configuration for assessing the BMSA methodology.

For the purpose of BMSA calibration, we extracted from LES data selected quantities of interest, namely, the tangential velocity and turbulent kinetic energy profiles in the wall-normal direction and total pressure profiles in the wake. The LES data are in good agreement with the experiments of [31]. Tangential velocity profiles at 4 streamwise positions (at $x/l = 0.56, 0.64, 0.76$ and 0.99 on the suction side, l being the chord and $x/l = 0$ the leading edge), and total pressure ($P_{t_{inlet}} - P_t)/(P_{t_{inlet}} - P_{inlet})$ profiles at 2 positions downstream of the trailing edge ($x/l = 1.02$ and 1.1) were used for the calibration/assessment of all models considered in the study. For RANS models involving a transport equation for the turbulent kinetic energy (TKE), such as the $k - \omega$ and $k - \varepsilon$ models, we also considered TKE profiles at the same positions on the suction side as the velocity profiles. For the calibrations reported in the following we used data for a small number of observation points along each profile, clustered in the near wall region and toward the wake center. The data are then concatenated to form the vector \bar{D} . In total, we used 82 probes for $k - \omega$ and $k - \varepsilon$ models, and 50 for Spalart–Allmaras model. As a general rule, the number of data used in the

calibration is a tradeoff between the necessity of informing the model coefficients and computational cost associated with the construction and inversion of the correlation matrices involved in the likelihood function.

3.2. Flow models

The flow around the compressor cascade is modelled by the compressible RANS equations (not reported for the sake of brevity) supplemented with a turbulence model. Since it is not possible to identify *a priori* the "best" turbulence model for predicting an unseen configuration based on pure expert judgement, we adopt a multi-model ensemble constituted of three concurrent turbulence models, briefly described thereafter. The reader may refer to the original references for more details. Only linear eddy viscosity models are considered in the following since, despite the limitations intrinsic to the so-called Boussinesq hypothesis, they are robust and widespread in industrial flow solvers. For such models, *a posteriori* estimates of the closure coefficients and of the posterior model probabilities determined from model calibrations against 14 flat plate flow scenarios have been made available in [3, 4]. These posteriors have been proven useful for prediction on different flows, such as pipes and wings.

3.2.1. Launder–Sharma $k - \varepsilon$

The $k - \varepsilon$ model of Launder and Sharma [26] relies on the solution of transport equations for the turbulent kinetic energy k and the turbulent dissipation ε for computing the eddy viscosity coefficient $\nu_t = C_\mu k/\varepsilon$. The transport equations and the eddy viscosity definition involve six uncertain closure coefficients: C_μ , $C_{\varepsilon 1}$, $C_{\varepsilon 2}$, σ_ε , σ_k and κ , with κ the von Karman constant. These are not all independent since they have to satisfy the fol-

lowing relationships, derived for simple canonical flows [34] (see also [3]):

$$\kappa^2 = \sigma_\varepsilon C_\mu^{1/2} (C_{\varepsilon 2} - C_{\varepsilon 1}) \quad (14)$$

$$\frac{P}{\varepsilon} = \frac{C_{\varepsilon 2} - 1}{C_{\varepsilon 1} - 1} \quad (15)$$

378 Following [35] we set $\frac{P}{\varepsilon} = 2.09$ in equation (15). By
 379 enforcing the preceding relationships, we are finally left
 380 with 4 uncertain closure coefficients, namely $C_{\varepsilon 2}$, C_μ ,
 381 σ_k and κ . The standard values of these coefficients for
 382 the Launder–Sharma model are given in Table 2.

3.2.2. Wilcox $k - \omega$ (2006)

The second model is Wilcox’ $k - \omega$ model [25], based on transport equations for the turbulent kinetic energy k and the turbulent dissipation rate $\omega = \varepsilon/k$. This model has seven closure coefficients denoted α , β , β^* , σ , σ^* , σ_{do} and κ , whose standard values are given in Table 2. The coefficients must satisfy the relation [25]

$$\alpha = \frac{\beta}{\beta^*} - \frac{\kappa^2}{2\sqrt{\beta^*}} \quad (16)$$

384 so that only six independent coefficients are left. In the
 385 following, α is computed *a posteriori* once the other co-
 386 efficients have been calibrated from data.

3.2.3. Spalart–Allmaras model

The Spalart–Allmaras model [24] is a single-transport-equation model for a viscosity-like quantity $\tilde{\nu}$, which merges with turbulent viscosity ν_t far from the walls. It involves 8 closure coefficients: C_{b1} , C_{b2} , σ , C_{w1} , C_{w2} , C_{w3} , C_{v1} and κ . Since the coefficient C_{w1} is related to the other coefficients by the relation:

$$C_{w1} = \frac{C_{b1}}{\kappa^2} + \frac{1 + C_{b2}}{\sigma} \quad (17)$$

388 only 7 independent closure coefficients are left, whose
 389 standard values are given in Table 2.

| Model | Closure Coefficient | Standard value |
|----------------------|---------------------|----------------|
| $k - \varepsilon$ | $C_{\varepsilon 2}$ | 1.92 |
| | C_μ | 0.09 |
| | σ_k | 1.0 |
| | κ | 0.41 |
| $k - \omega$ | κ | 0.41 |
| | σ_{do} | 0.125 |
| | σ^* | 0.6 |
| | σ | 0.5 |
| | β^* | 0.09 |
| | β | 0.0708 |
| | κ | 0.41 |
| Spalart- Allmaras | C_{w2} | 0.3 |
| | C_{w3} | 2.0 |
| | C_{v1} | 7.1 |
| | C_{b1} | 0.1355 |
| | C_{b2} | 0.622 |
| | σ | 2/3 |

Table 2: Standard values of the closure coefficient for the $k - \varepsilon$, $k - \omega$ and Spalart–Allmaras models, according to [26] [25] [24], respectively.

3.3. RANS solver and computational setup

390 The simulations presented in this study are con-
 391 ducted by using the CFD solver *elsA*, developed by
 392 ONERA [36]. We solve the 2D steady compressible
 393 RANS equations for perfect Newtonian gases by using
 394 a cell-centered finite volume approximation on struc-
 395 tured multi-block grids. The upwind scheme of Roe
 396 with second-order MUSCL extrapolation is used for ap-
 397 proximating the spatial fluxes. For time stepping, we
 398 use the first-order backward Euler scheme.

399 The computational domain contains a single blade
 400 profile and periodic boundary conditions are applied at

402 the upper and lower boundaries to simulate an infinite
403 cascade. The domain extends from 0.4 chords upstream
404 of the leading edge to 0.5 chords downstream the trail-
405 ing edge. The top and bottom boundaries are separ-
406 ated by a distance equal to the gap between neighbor-
407 ing blades, $t/l = 0.59$, with l the axial chord. In addi-
408 tion to the periodicity conditions at the upper and lower
409 boundaries, non-slip adiabatic boundary condition is ap-
410 plied at the blade wall, and characteristic conditions are
411 imposed at the inlet and outlet boundaries. At the in-
412 let, the total pressure, enthalpy and angle of attack are
413 prescribed; a constant static pressure is enforced at the
414 outlet. The computational grid is composed by 200,000
415 cells distributed on 12 blocks. The near-wall grid reso-
416 lution leads to an average height of the first cell closest
417 to the wall (in wall coordinates) such that $y^+ < 1.0$ on
418 both the suction and the pressure side of the blade. For
419 all computations, we assume that the solution has con-
420 verged to the steady state when the L_2 norm of the resid-
421 uals is reduced by five order of magnitude with respect
422 to the initial value. The simulations are run in paral-
423 lel on 12 cores and the typical CPU time for obtaining a
424 converged solution is of the order of 20 minutes. Since a
425 very large number of numerical simulations is required
426 for the calibration of model coefficients using MCMC,
427 the solver output for the observed data is approximated
428 by means of a surrogate model, described in the next
429 section.

430 3.4. Surrogate modelling

To reduce the number of expensive RANS simula-
tions involved in model calibrations, we approximate
the QoIs required in the argument of the likelihood func-
tion, (*i.e.* $\Delta(\theta)$) by means of surrogate models based
on Gaussian process regression. For that purpose, we

use the Gaussian Process Regression module available
in *scikit-learn* [37]. We select a *Matern* – 3/2 kernel,
whose hyperparameters are determined by optimizing
the likelihood. For that purpose, we use the L-BFGS-
B [38] optimizer available in the *scipy* library [39]. The
initial RANS calculations required as an input to the sur-
rogate model are distributed in the parameter space by
Latin Hypercube Sampling (LHS) [40] optimized un-
der the Maximum Projection Design criterion. More
precisely, this criterion ensures optimal space filling by
maximizing the minimal distance between points of the
LHS, for every projection in parameter sub-spaces. We
construct a separate surrogate based on 200 RANS sam-
ples for each concurrent turbulence model and each cal-
ibration scenario in Table 1, for a total of 2400 CFD
calculations, run in parallel on a multi-processor com-
puter. This is a considerable computational effort, but it
is done one for all prior to the calibration phase. For a
given model and a given scenario, the 200 samples are
used to build a surrogate for each one of the observed
QoIs involved in the likelihood function (namely, veloc-
ity, TKE and total pressure values at selected points in
the flow field, as discussed in section (3.1)). We ver-
ified the accuracy of the surrogate models by Leave-
One-Out cross-validation. For each model and scenario,
we compute the Q_n^2 criterion for every element Δ_n of
 $\Delta = (\Delta_1, \dots, \Delta_N)$. By definition, Q_n^2 is defined as :

$$Q_n^2 = 1 - \frac{\frac{1}{200} \sum_{i=1}^{200} \left((\Delta_n)_i^{true} - (\Delta_n)_i^{pred} \right)^2}{Var((\Delta_n)^{true})} \quad (18)$$

431 For each model and scenario, we present in Table 3 the
432 mean value of the Q_n^2 criterion, averaged on the N sur-
433 surrogate models.

| Average Q^2 | $k - \varepsilon$ | $k - \omega$ | Spalart–Allmaras |
|---------------|-------------------|--------------|------------------|
| S_1 | 0.976 | 0.991 | 0.975 |
| S_2 | 0.967 | 0.968 | 0.965 |
| S_3 | 0.995 | 0.997 | 0.970 |
| S_4 | 0.996 | 0.985 | 0.994 |

Table 3: Average values of Q_n^2 for models and scenarios.

4. Results

In this section, BMSA is used to predict two of the scenarios presented in section 3.1 (namely, S_2 and S_4). In scenario S_2 , the flow remains attached all over the suction side of the blade, whereas flow separation is observed in scenario S_4 , which is very different from the other scenarios in the database and represents a challenging configuration for assessing BMSA predictions far outside the training set. The BMSA results reported in the following are based on different ensembles of calibration scenarios. First, a baseline BMSA model, noted BMSA1, is constructed by propagating the *maximum-a-posteriori* (MAP) estimates of model coefficients and the model posterior probabilities of [4]. Although such coefficients were obtained for flat plate flows, we may expect that the thin NACA65 V103 blades can be approximately modelled as flat plates subject to a variable (mostly adverse) pressure gradient. It is then interesting to measure the capability of BMSA to predict the present compressor cascade before having observed any data for this family of configurations. In the following, the flat-plate scenarios are noted S_{XYZW} , with $XYZW$ the four-digit code assigned to the scenarios in [3], to which we refer for more information.

Afterwards, another BMSA model, noted BMSA2, is developed by calibrating the RANS models against

compressor configurations. More precisely, we calibrate the models against data available for each of the four compressor scenarios of Sec. 3.1 and we determine the corresponding model evidences. Then, we construct BMSA models of S_2 and S_4 by using the three remaining scenarios. For instance, we use models trained on scenarios S_1 , S_3 and S_4 to predict scenario S_2 .

Finally, a more general BMSA model, named BMSA3, is constructed by mixing together flat plate scenarios and the S_1 , S_2 and S_3 NACA 65 scenarios and applied to the prediction of S_4 .

In all cases the smart scenario weighting of Eq. (13) is used to assign *a priori* probabilities to the scenarios involved in the BMSA models.

Specifically, the error term ϵ_k in Eq. (13) is determined by computing the $\|\cdot\|_2$ of local errors on the normalized velocity and total pressure profiles at the streamwise stations of section 3.

4.1. Calibration results

In order to construct a BMSA model specifically trained for compressor configurations, we apply the statistical calibration framework described in section 2.1 to infer on the parameters of the RANS models for the scenarios of section 3.1.

For each model and scenario, we assign to the closure coefficients non-informative uniform marginal distributions priors initially ranging from 10% to 250% of the standard values described in Table 2. For some models and scenarios, these large ranges are eventually restricted to values preventing the CFD solver to converge.

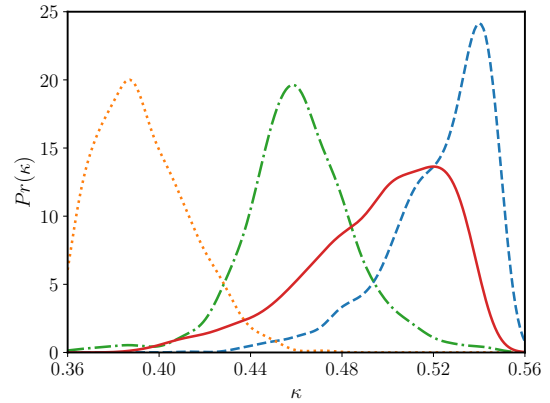
The hyper-parameter σ_η is assigned a uniform prior in the range $[0, 1]$. For illustrative purpose, we present

493 in Table 4 the prior ranges for the closure coefficients of
 494 Spalart–Allmaras model and scenario 3.

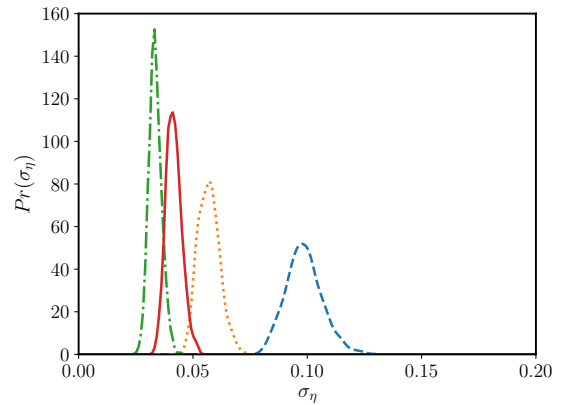
| Closure Coefficient | Lower bound | Upper bound |
|---------------------|-------------|-------------|
| κ | 0.36 | 0.56 |
| C_{w2} | 1.0 | 2.4 |
| C_{w3} | 0.1 | 0.9 |
| C_{v1} | 6.5 | 18.0 |
| C_{b1} | 0.5 | 1.5 |
| C_{b2} | 0.06 | 0.16 |
| σ | 0.6 | 2.0 |

Table 4: Lower and upper bounds for the prior of the Spalart–Allmaras closure coefficient for the scenario 3.

495 Figure 2a shows typical calibration results for the κ
 496 coefficient of the Spalart–Allmaras model. As also ob-
 497 served in [41], the coefficient is well informed by the
 498 data but is highly sensitive to the calibration scenario.
 499 It can be noticed that calibration may assign high prob-
 500 abilities to values of κ that are very different from the
 501 standard value 0.41, especially for off-design scenarios
 502 farthest from the nominal conditions. Similar results are
 503 obtained for other coefficients and models, not reported
 504 for brevity. In the next Figure 2b, we present calibra-
 505 tion results for the hyper-parameter σ_η , which is also
 506 well informed by the data. As described in Section 2.1,
 507 σ_η can be interpreted as a measure of model accuracy
 508 in the calibration scenario. We notice that for all cali-
 509 brations the mean of the hyper-parameter σ_η is smaller
 510 than 10%.



(a) Coefficient κ .



(b) Hyper-parameter σ_η .

Figure 2: Posterior probabilities in case of Spalart–Allmaras model: Scenario 1 (— — —), Scenario 2 (· · · · ·), Scenario 3 (— · — ·) and Scenario 4 (— — —). Priors has been chosen uniform on [0.36 , 0.56] and [0 , 1] respectively.

4.2. BMSA prediction for S_2

For the rest of this paper, we present BMSA prediction in blue color, with first and second standard deviations in degrading shades of blue. Red color is reserved for the LES reference data from [1]. Black, green and orange colors are used respectively for the baseline $k - \omega$, $k - \epsilon$ and Spalart–Allmaras models, with the nominal closure coefficients of Table 2.

In this section we first report results of BMSA of the

520 NACA65 V103 configuration at mildly off-design con- 555
521 ditions, namely, scenario S_2 . The results are discussed 556
522 for selected velocity and total pressure profiles, repre- 557
523 sentative of typical BMSA predictions. However, simi-
524 lar considerations hold for other locations in the flow.

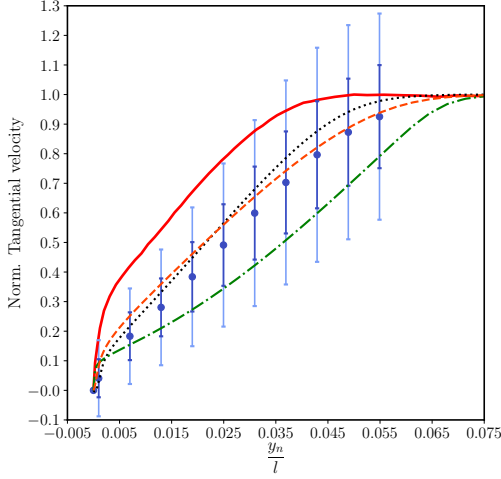
525 We present in Figure 3 the tangential velocity profile
526 at $x/l = 0.99$. The x -axis represents the normalized dis-
527 tance to the wall y_n/l , y_n being the distance to the blade.
528 The BMSA results are based on the three sets of scenar-
529 ios described in the above. Predictions of the baseline
530 RANS models are also reported for comparison. These
531 exhibit significant differences, even for the present at-
532 tached 2D flow. The $k - \omega$ and Spalart–Allmaras mod-
533 els provide rather close predictions, in better agreement
534 with the LES data than the $k - \epsilon$ model, which performs
535 noticeably worse than the two other for this case. 558

536 Figure 3a displays results for the BMSA1 model, *i.e.* 559
537 using on-the-shelf MAP estimates of model coefficients 560
538 calibrated on flat plates from [4]. The prediction ex- 561
539 pectancy for this model does not yield better results than 562
540 the best baseline model but performs much better than 563
541 the worst one. Moreover, the prediction error bars, cor- 564
542 responding to ± 2 standard deviations, encompass rather 565
543 well the reference data, except in the region closest to 566
544 the wall. 567

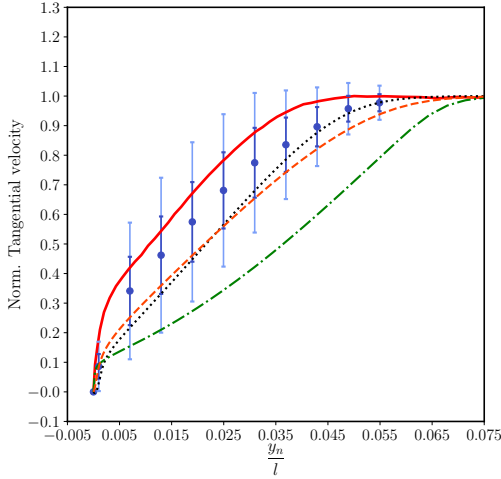
545 In Figure 3b we report the results for BMSA2, cali- 568
546 brated on compressor scenarios $\{S_1, S_3, S_4\}$ and applied 569
547 to S_2 . In this figure, the complete posterior distribu- 570
548 tions are propagated through the models based on krig- 571
549 ing surrogates of the output QoI. Propagation of the full 572
550 posterior distributions is based on surrogate models for 573
551 each RANS model in the mixture and each QoI, as dis- 574
552 cussed in the above. The predictive accuracy of BMSA 575
553 improves significantly when we consider closeby sce- 576
554 narios for model calibrations. In particular, the mean 577

prediction $E[\Delta|S']$ is significantly better than the best
RANS model, and the reference data are now captured
within only one standard deviation.

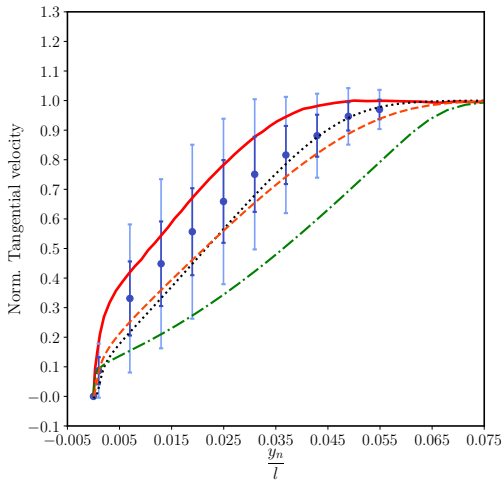
The cost of the kriging surrogate increases with the
size of the parameter space but can be roughly estimated
to $O(10P)$, with P the number of uncertain parameters.
A way of reducing the computational overcost associ-
ated with the propagation step is to approximate the full
posterior distributions with MAP estimates of the co-
efficients. Using this approximation neglects the pos-
terior parametric uncertainty but involves only $K \times I$
RANS calculations using the MAP estimates for the
coefficients. Furthermore, since the parameters are no
longer considered as random variables in the propaga-
tion step, the BMSA formula can be applied to any QoI
in the output solution and not only to selected QoI and
flow locations for which a surrogate is available. Fig-
ure 3c reports results for BMSA2 based on the propaga-
tion of MAP estimates of the coefficients for scenarios
 $\{S_1, S_3, S_4\}$ through scenario S_2 . It turns out that the
BMSA prediction using MAP estimates is very close to
the one using the full posteriors, both in terms of ex-
pectancy and of standard deviation.



(a) MAP estimates calibrated on flat-plate [4].



(b) Complete distributions obtained on $\mathcal{S} = \{S_1, S_3, S_4\}$.



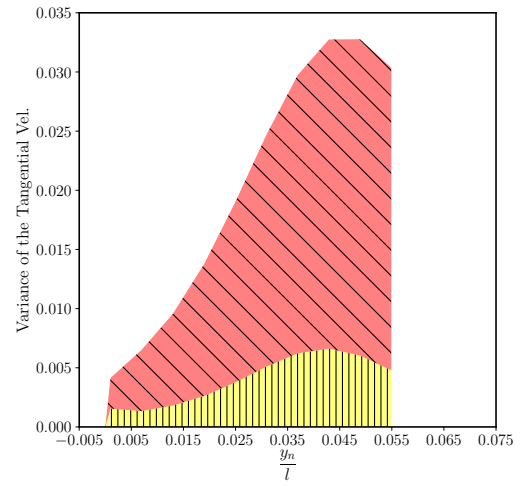
(c) MAP estimates obtained on $\mathcal{S} = \{S_1, S_3, S_4\}$.

Figure 3: Prediction of the normalized tangential velocity profile at $x/l = 0.99$ on the suction side for scenario 2. LES data from Leggett et al. [1] (—), $E[\Delta|S'] \pm \sqrt{\text{Var}[\Delta|S']}$ (—●—), $E[\Delta|S'] \pm 2\sqrt{\text{Var}[\Delta|S']}$ (—●—), Baseline $k - \omega$ (·····), Baseline Spalart–Allmaras (---) and Baseline $k - \varepsilon$ (-·-·).

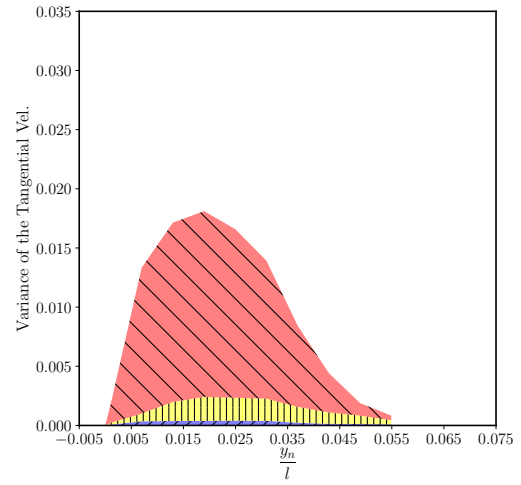
578 Figure 4 shows the variance decomposition according to equation 9, for each prediction of Figure 3. The total variance for BMSA1 is larger than for the other two cases, due to the greater diversity of scenarios included in the model. The wall-normal locations associated with the largest variance is close to the boundary layer edge in this case, whereas it is located in the near-wall region for BMSA2 predictions, either using full posteriors and MAP estimates. A possible explanation is that the flat-plate scenarios used in BMSA1 mostly differ in the wake region. As a consequence, the calibration mostly adjusts the coefficients to fit velocity profiles in the outer part of the boundary layer. On the contrary, for NACA65 scenarios the near wall region is found to be the most sensitive to the RANS model.

589 As expected, the *within-model, within scenario* variance is strictly equal to zero for the MAP-based BMSA models. However, inspection of Figure 4b shows that this term is also very small when propagating the full posteriors. The reason is that the latter are rather peaked (*i.e.* not too far from a Dirac function), since the model coefficients are well informed from the data. The residual parametric uncertainty is then negligible compared to the *between-model, within scenario*. On the other hand, the total variance of the MAP-based BMSA2 model (Figure 4c) is comparable to the one of the full BMSA2 or slightly larger. The discrepancy is due to the different probabilities assigned to the scenarios in the two cases, which are discussed below. Overall, these results further support the choice of MAP estimates for BMSA predictions. To complete the discussion of this figure, we also observe that the larger contribution to the variance is due to the *between scenarios* component. This indicates that the uncertainty associated with the calibration of the closure coefficients

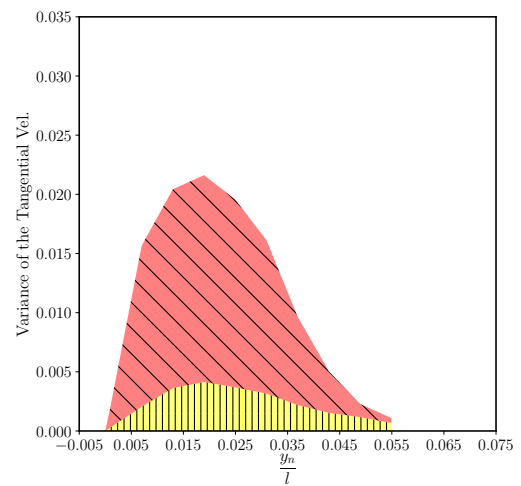
613 against different datasets is larger than the uncertainty
 614 about the more suitable model form.



(a) MAP coefficients calibrated on flat-plate [4].



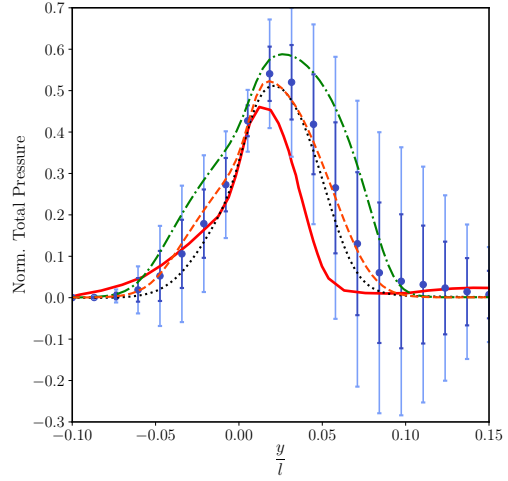
(b) Complete distributions obtained on $\mathcal{S} = \{S_1, S_3, S_4\}$.



(c) MAP coefficients obtained on $\mathcal{S} = \{S_1, S_3, S_4\}$.

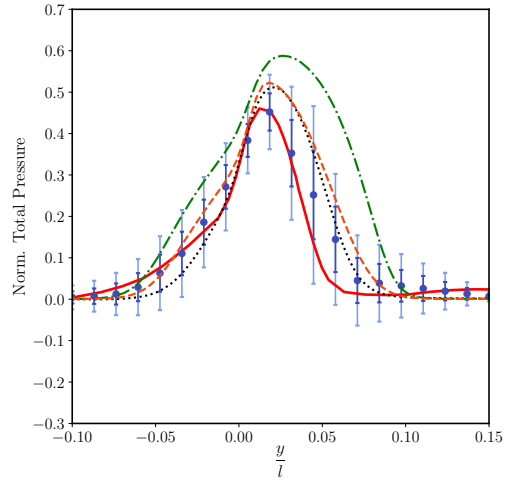
Figure 4: Variance decomposition of prediction for the normalized
 15 tangential velocity profile on the suction side at $x/l = 0.99$ for sce-
 nario 2. ■ within-model, within scenario variance, ■ between mod-
 els, within scenario variance and ■ between scenario variance

615 BMSA predictions of a normalized total pressure pro-
 616 file in the compressor wake are presented in Figure 5.
 617 Results are reported again for BMSA1 and for BMSA2
 618 based on full posterior distributions and MAP estimates
 619 of the coefficients. The quantity on the x -axis (namely
 620 y/l) represents the normalized crossflow position, with
 621 the origin aligned with the trailing edge.

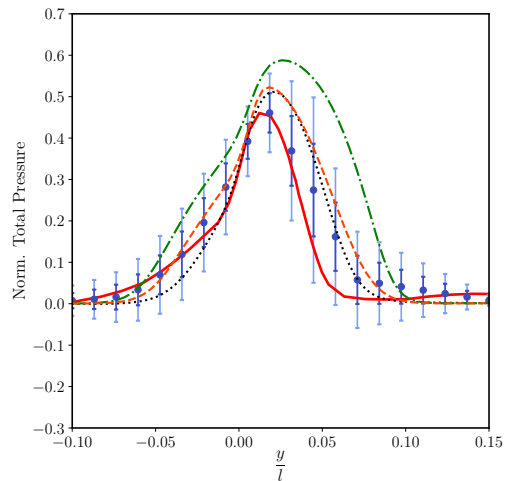


(a) MAP coefficients calibrated on flat-plate [4].

622 For this QoI, the BMSA models exhibit a behavior
 623 similar to the velocity profiles. Specifically, the $k - \epsilon$
 624 baseline model predicts a wake profile farther from the
 625 LES reference compared to the two other baselines.
 626 Second, the prediction using the BMSA1 model pre-
 627 dicta a wake profile relatively close to the best perform-
 628 ing nominal RANS model, with LES reference data
 629 falling within two standard deviations from the mean
 630 prediction. As for the velocity profile, the BMSA2
 631 model provides results in very good agreement with the
 632 reference data (Figure 5b), especially for the peak and
 633 the left-hand side of the profile. For the right-hand side,
 634 corresponding to flow coming from the suction side
 635 (characterized by a more challenging physics), BMSA
 636 still improves over the nominal models but with higher
 637 standard deviations than for the rest of the profile. The
 638 results do not change much when using MAP estimates
 639 instead of full posteriors. In fact, Figure 6 shows that,
 640 once again, the contribution of parametric uncertainty to
 641 the total variance is very small, which justifies the use
 642 of MAPs.



(b) Complete distributions obtained on $\mathcal{S} = \{S_1, S_3, S_4\}$.



(c) MAP coefficients obtained on $\mathcal{S} = \{S_1, S_3, S_4\}$.

Figure 5: Prediction of the normalized pressure wake profile at $x/l =$
 16 1.10 for scenario 2. LES data from Leggett *et al.* [1] (—), $E[\Delta|S'] \pm$
 $\sqrt{\text{Var}[\Delta|S']}$ (—●—), $E[\Delta|S'] \pm 2\sqrt{\text{Var}[\Delta|S']}$ (—●—), Baseline $k - \epsilon$
 (·····), Baseline Spalart-Allmaras (— · — ·) and Baseline $k - \epsilon$ (— · — ·).

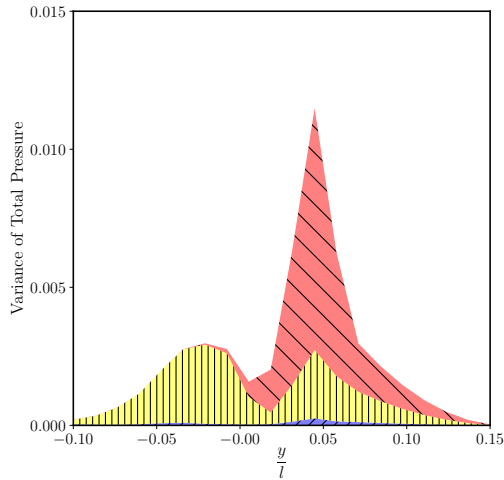
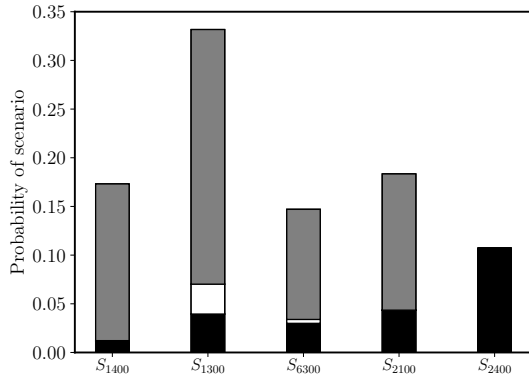


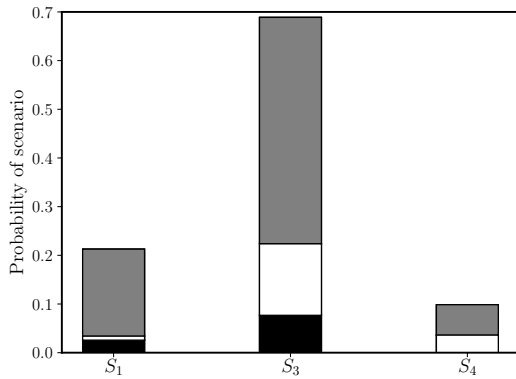
Figure 6: Variance decomposition of prediction for the normalized pressure wake profile at $x/l = 1.10$ for scenario 2 for the complete distributions obtained on $\mathcal{S} = \{S_1, S_3, S_4\}$. ■ *within-model, within scenario variance*, ■ *between models, within scenario variance* and ■ *between scenario variance*

643 Finally, in Figure 7 we compare the scenario weight-
644 ing for the various scenarios. Only scenarios that are as-
645 signed a probability of 5% or more are shown. For each
646 scenario, we also report the fraction assigned to each
647 RANS model in the mixture, *i.e.* $P(M_i | \overline{D}_k, S_k) P(S_k)$
648 For BMSA1, the calibration scenarios are labelled as in
649 [3]. The scenario weighting criterion automatically as-
650 signs higher probabilities to scenarios corresponding to
651 mixed pressure gradients (airfoil-like cases like S_{2100})
652 or to zero-gradient (S_{1400}) and mildly favorable cases
653 (S_{6300}), which is a bit counter-intuitive. This is proba-
654 bly due to the fact that model agreement for the predic-
655 tion scenarios is better for regions of favorable pressure
656 gradient (the left part of the blade), leading to lower er-
657 rors and the higher weighting of such scenarios. For
658 BMSA2, scenario weighting is little affected by the
659 MAP approximation. In both cases, the scenarios are
660 assigned similar probabilities, with scenarios S_1 and S_3
661 being preferentially weighted with respect to S_4 . This

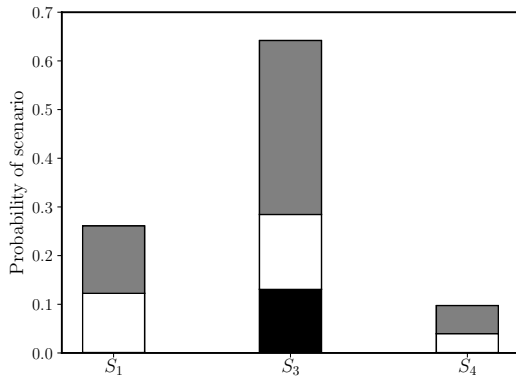
662 can be explained by the proximity of the inlet flow angle
663 of S_2 , S_3 and S_1 . For the first two scenarios, the flow
664 is qualitatively similar to S_2 , which is not the case for
665 S_4 , as discussed in the next section. In all BMSA, the
666 Spalart–Allmaras model is generally assigned the high-
667 est probability, and $k - \epsilon$ the lowest. Using the MAP ap-
668 proximation changes slightly the model evidences, and
669 subsequently model weighting within each scenario, but
670 the results are overall very close to the BMSA2 using
671 the full posterior distributions.



(a) MAP coefficients calibrated on flat-plate [4]

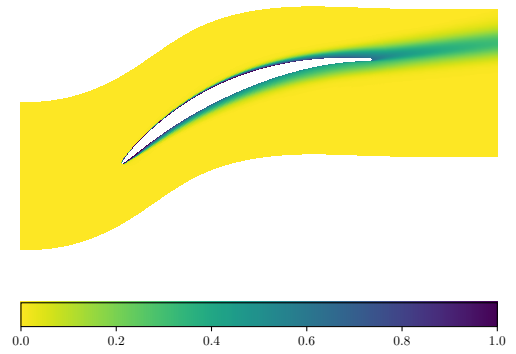


(b) Obtained with complete distributions on $\mathcal{S} = \{S_1, S_3, S_4\}$.

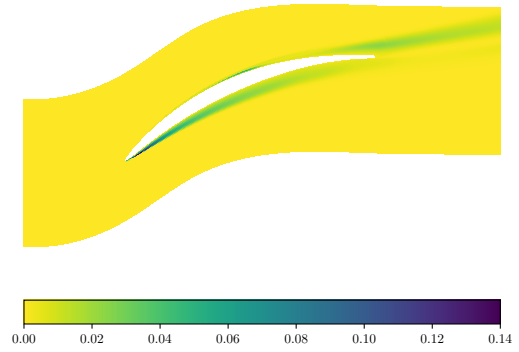


(c) Obtained with MAP estimates of the distributions on $\mathcal{S} = \{S_1, S_3, S_4\}$.

Figure 7: Distribution of $p(S_k)$ and $p(M_i|\overline{D}_k, S_k)$ in case of scenario 2. Only scenarios with probability superior to 5% are shown on Figure 7a. Each bar sums to the probability of the scenario. Each probability of scenario is then decomposed into probabilities of models, given this scenario. $k - \varepsilon$ (■), $k - \omega$ (□) and Spalart-Allmaras (▒).



(a) $E [P_t(x_i)|S_2]$



(b) $Var [P_t(x_i)|S_2]$

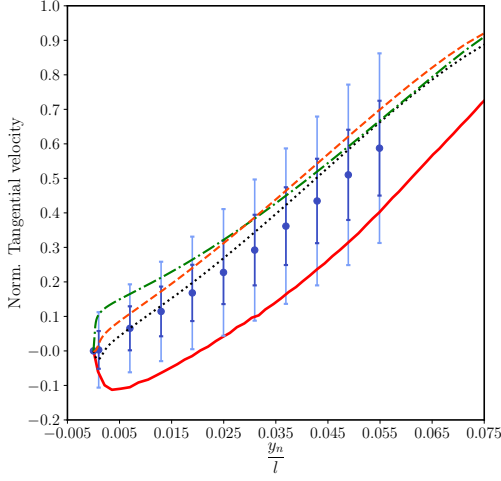
Figure 8: 2-D contour of first two moments of the BMSA prediction for normalized total pressure for scenario 2. In this case, we considered MAP estimates on scenarios $\mathcal{S} = \{S_1, S_3, S_4\}$

672 A clear advantage of the MAP approximation of the
 673 posteriors, in addition to speeding up the prediction
 674 phase, is that it allows constructing a BMSA predic-
 675 tion for any QoI in the flow, compared to the surrogate-
 676 based propagation. For instance, Figure 8 shows the
 677 iso-contours of the mean and standard deviation of the
 678 total pressure field around the blade. The latter provides
 679 a global view of flow regions that are the most sensitive
 680 to the turbulence model. Based on the preceding discus-
 681 sion, only MAP-based BMSA models are considered in
 682 the following.

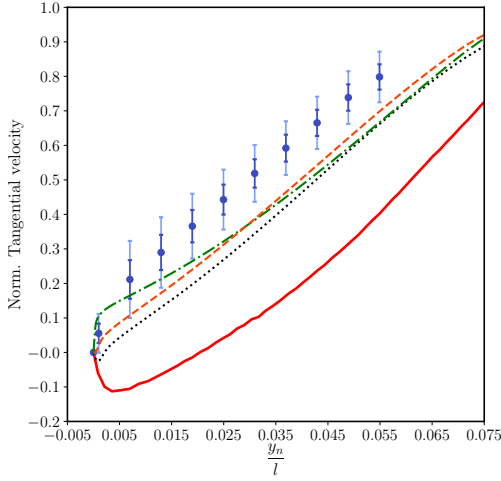
683 4.3. BMSA prediction for S_4

684 The BMSA mixture models are then applied to the
685 prediction of a more challenging off-design conditions,
686 *i.e.* the separated flow scenario S_4 . We show in Fig-
687 ure 9 the predictions for the tangential velocity profile
688 at $x/l = 0.99$ on the suction side in this case. The
689 BMSA1 solution is reported in Figure 9a. The solu-
690 tion clearly under-estimates the size of the backward
691 flow region. Nevertheless, the predicted velocity pro-
692 file exhibits incipient separation and the $\pm 2\sigma$ error bars
693 encompass reasonably well the reference LES solution.
694 Figure 9b reports results for BMSA2 calibrated on sce-
695 narios S_1, S_2 and S_3 . In this case, the mean solution
696 compares poorly with the reference LES. Since BMSA2
697 has been calibrated on attached scenarios, the posterior
698 coefficients tend to provide even fuller velocity profiles
699 than the baseline models, which already fail to predict
700 flow separation, except for the baseline $k-\omega$ that under-
701 estimates the size of the reversed flow. We also observe
702 that, in this case, the error bars are small and do not en-
703 compass the reference data. This is due to the fact that
704 the models in the mixture strongly agree on the wrong
705 solution. This result shows the importance of including
706 sufficientlly diverse scenarios in BMSA models. In the
707 present BMSA, predictions are based on models with
708 similar characteristics (linear eddy viscosity), further-
709 more calibrated on similar attached flow scenarios. As a
710 consequence, the resulting BMSA model is very good at
711 predicting flow scenarios similar to the calibration ones
712 but generalizes badly to a different flow, leading to less
713 accurate results than BMSA1. In Figure 9c we present
714 results for BMSA3, which aggregates together the flat
715 plate scenarios and the NACA65 scenarios. Increasing
716 the diversity of scenarios in the model mixture has a
717 beneficial effect on the solution, which is not worst than

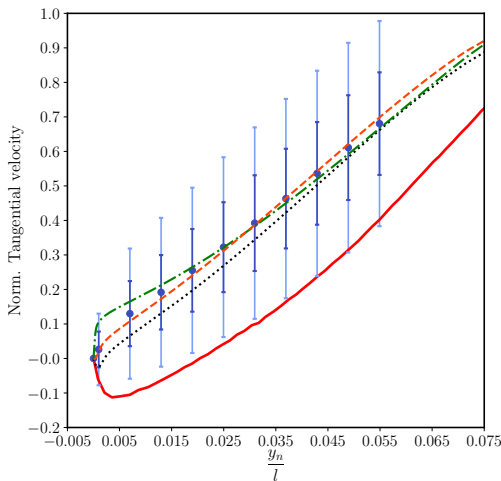
718 the baseline RANS models in the average, but provides
719 an estimate for the error bars. The reference data are
720 captured within approximately two standard deviations
721 from the average.



(a) MAP estimates calibrated on flat-plate [4].



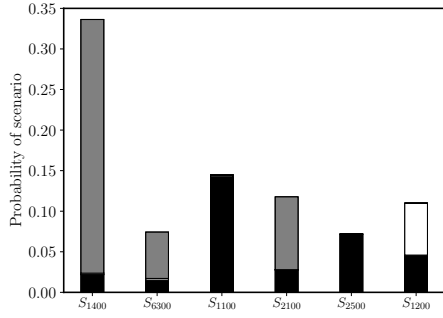
(b) MAP estimates obtained on $\mathcal{S} = \{S_1, S_2, S_3\}$.



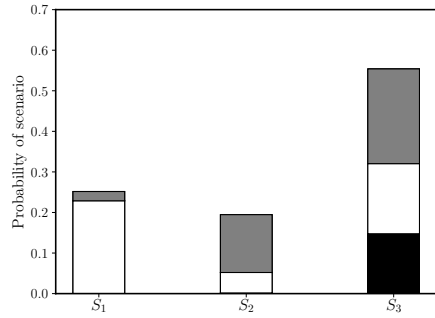
(c) MAP estimates obtained on $\mathcal{S} = \{S_{1400}, \dots, S_{2134}, S_1, S_2, S_3\}$.

722 The scenario probabilities are reported in Figure 10
723 for the three BMSA. Once again we focus only on sce-
724 narios with a probability of 5% or higher. For BMSA1
725 (10a), the most influential scenario is S_{1400} , *i.e.* the
726 zero pressure gradient flat plate, probably due to strong
727 model agreement in the upstream portion of the flow.
728 Interestingly, the BMSA now also assigns significant
729 weights to S_{1100} and S_{2500} , characterized by mildly ad-
730 verse pressure gradients, and S_{1200} which is representa-
731 tive of a "diverging channel, with eventual separation".
732 Such scenarios were not assigned any significant proba-
733 bility in the S_2 solution. For BMSA2, the highest proba-
734 bility is assigned to S_3 , followed by S_1 and finally S_2 .
735 This shows that the scenario weighting criterion tends
736 to promote scenarios with inlet angles closest to the
737 one of the prediction scenario. Finally, BMSA3 (Fig-
738 ure 10c) assigns the higher weights to the mixed and
739 adverse pressure gradient scenarios from BMSA1 and
740 to the NACA65 scenarios.

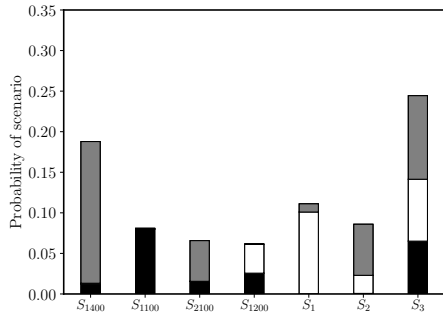
Figure 9: Prediction of the tangential velocity profile at $x/l = 0.99$ on
the suction side for scenario 4. LES data from Leggett *et al.* [1] (—),
 $E[\Delta|S'] \pm \sqrt{\text{Var}[\Delta|S']}$ (—●—), $E[\Delta|S'] \pm 2\sqrt{\text{Var}[\Delta|S']}$ (—●—), Base-
line $k-\omega$ (·····), Baseline Spalart–Allmaras (— · —) and Baseline $k-\varepsilon$
(— · · —).



(a) MAP coefficients calibrated on flat-plate [4].



(b) MAP estimates obtained on $S = \{S_1, S_2, S_3\}$.



(c) MAP estimates obtained on $S = \{S_{1400}, \dots, S_{2134}, S_1, S_2, S_3\}$.

Figure 10: Distribution of $p(S_k)$ and $p(M_i|\overline{D}_k, S_k)$ in case of scenario 4. Only scenarios with probability superior to 5% are shown on Figures 10a and 10c. Each bar sums to the probability of the scenario. Each probability of scenario is then decomposed into probabilities of models, given this scenario. $k-\varepsilon$ (■), $k-\omega$ (□) and Spalart–Allmaras (▣).

| | Scenario 2 | | Scenario 4 | |
|-----------------------|-------------|-------------|-------------|-------------|
| | $U_{t,RMS}$ | $P_{t,RMS}$ | $U_{t,RMS}$ | $P_{t,RMS}$ |
| Baseline | 0.728 | 0.492 | 0.797 | 0.345 |
| Flat plate | 0.710 | 0.448 | 0.567 | 0.232 |
| NACA65 configuration | 0.275 | 0.183 | 1.199 | 0.554 |
| NACA65 and flat plate | 0.561 | 0.356 | 0.843 | 0.372 |

Table 5: Root-Mean Square values for the baseline models (averaged value for the 3 considered models), BMSA with models calibrated on flat plates [4], BMSA with models calibrated on NACA65 configurations and BMSA with models calibrated on NACA65 and flat plates together.

741 5. Conclusions

742 A recently developed Bayesian framework is as-
743 sessed for the quantification and reduction of modelling
744 uncertainties in RANS-based simulations of turboma-
745 chinery flows. In this framework, modelling uncertain-
746 ties are treated in terms of probabilities. Specifically,
747 the closure coefficients associated with RANS models
748 are treated as random variables, which are assigned an
749 a priori probability distribution based on their nominal
750 values and expert judgement. Bayesian inference from
751 observed data for selected Quantities of Interest (QoI) is
752 used to reduce the uncertainty ranges of the coefficients,
753 leading to a posteriori distributions. The latter can be
754 propagated through the model by means of an Uncer-
755 tainty Quantification (UQ) method to obtain predictions
756 with quantified uncertainty of a new flow. Additionally,
757 the proposed framework leverages information from a
758 set of concurrent RANS models and a set of concurrent
759 calibration scenarios to build a mixture model based on
760 Bayesian-Model-Scenario-Averaging (BMSA). BMSA

allows to account to some extent for uncertainties associated with the mathematical form of the RANS model and for uncertainties associated with the choice of flow scenarios for model calibration in view of the stochastic prediction of a new flow not included in the calibration set.

BMSA models were constructed by averaging three linear-eddy viscosity models widely used for industrial applications, namely, Spalart–Allmaras, Wilcox’ $k - \omega$ and Launder–Sharma $k - \varepsilon$. A baseline mixture model, named BMSA1, was constructed by using on-the-shelf sets of model coefficients calibrated for fourteen turbulent flat-plate flow scenarios corresponding to different external pressure gradients [3, 4]. A second model, named BMSA2, was specifically tailored for the targeted flow configuration, *i.e.* the compressor cascade NACA65 V103. In this case, each RANS model in the mixture was calibrated against reference LES data [1, 2] available for 3 off-design scenarios and validated against data available for a fourth scenario, not included in the calibration set. The main parameter differentiating the scenarios is the flow inlet angle. The resulting posterior distributions of the model coefficients assign high probability to radically different values of the coefficients than the nominal values. The results show that, even if BMSA1 was not calibrated for the flows of interest, the results obtained for a mildly off-design and a highly off-design scenario are globally not worst than the nominal models and the estimated error bars encompass rather well the reference solution. On the other hand, the compressor-specific BMSA2 model significantly improves the predictions compared to the baseline RANS models when it is used to predict scenario characterized by an intermediary inlet angle with respect to those included in the BMSA. Additionally,

the predicted error bars encompass the reference data. However, this strategy may leads to overfitting problems. When applied to a scenario with operating conditions leading to radically different flow features compared to the training scenarios, BMSA provides less accurate predictions than the baseline models. In addition, the error bars are strongly underestimated due to the insufficient diversity of models and scenarios included in the mixture.

Since it is difficult to select *a priori* the most suitable scenarios to be included in the BMSA based on pure expert judgement (for instance, one could argued that flat plate scenarios are *a priori* less suitable than the NACA65 scenarios to predict another NACA65 flow condition), it is very important to include in the mixture sufficiently diverse flow scenarios and RANS model to mitigate overfitting and avoid underestimation of variance. For instance, predictions of the strongly off-design scenario based on a mixture of the flat plate and NACA65 scenarios preserved or improved the average prediction with respect to the baseline RANS models and delivered sufficiently large error bars to encompass the reference data.

A serious limitation to the number of models and scenarios in a BMSA is the computational cost of the stochastic prediction. In fact BMSA combines stochastic predictions of a new flow scenarios from K several models using posterior pdf of the closure coefficients calibrated for I flow scenarios. Each stochastic prediction involves an UQ calculation, corresponding to a high number ($O(100)$ or more, according to the UQ method in use and to the number of uncertain coefficients), leading to an unacceptably high number of costly deterministic RANS simulations, $O(100 K \times I)$. A first method for drastically reducing the required number of determinis-

831 tic simulations, first proposed in [4] and further assessed 866
832 in this work, is to approximate the posterior pdf by 867
833 Dirac pdf based on Maximum A Posteriori (MAP) es- 868
834 timates of the closure coefficients. This approximation 869
835 is shown to affect weakly the quality of the BMSA pre-
836 dictions, both in terms of mean and variance, while re- 870
837 ducing the number of deterministic simulations to only
838 $K \times I$, *i.e.* nine deterministic simulations in the present 871
839 application. All the required simulations are indepen- 872
840 dent and can be run in parallel and the BMSA intervenes 873
841 as a post-processing step. Since MAP-based BMSA 874
842 does not rely on any surrogate model for the UQ propa-
843 gation step, it can be use to extract potentially any QoI 875
844 at any point in the flow, provided that such QoI is com-
845 putable with the baseline models in the mixture (for in- 876
846 stance, a BMSA prediction of a QoI like the turbulent 877
847 kinetic energy k or the turbulent dissipation ε can be ob- 878
848 tained only if all the models in the mixture are at least 879
849 two-transport equation models). 880

850 Further reduction of the computational cost can be 881
851 achieved by using alternative criteria to assign weights 882
852 to the BMSA scenarios. In this work, we used a crite- 883
853 rion based on model agreement in the prediction sce- 884
854 nario derived in [3, 4]. This criterion has proved to 885
855 be effective in assigning high weights to scenarios in 886
856 the mixture that are more similar to the prediction case. 887
857 However, this criterion requires computing the new flow 888
858 with the K models using the coefficient from all of the 889
859 I scenarios, even when many of them are in the end as- 890
860 signed a very low probability. Alternative criteria have 891
861 been proposed in the literature (e.g. [27]) that allow 892
862 selecting the more suitable scenarios *a priori*, thus ex- 893
863 cluding from the beginning scenarios that are affected a 894
864 probability below a given threshold and finally reduc- 895
865 ing the number of deterministic calculations required 896

for the prediction of a new flow. The development and assessment of smarter and computationally efficient scenario-selection criteria will make the object of further research.

870 Acknowledgements

The authors acknowledge the french National Agency for Research and Technology (ANRT) for providing support through the CIFRE PhD grant number 2018-1370.

875 References

- [1] J. Leggett, S. Priebe, R. Sandberg, V. Michelassi, and A. Shabbir. Detailed investigation of rans and les predictions of loss generation in an axial compressor cascade at off design incidences. In *ASME Turbo Expo 2016: Turbomachinery Technical Conference and Exposition*. American Society of Mechanical Engineers Digital Collection, 2016.
- [2] J. Leggett. *Detailed investigation of loss prediction of an axial compressor cascade at off-design conditions in the presence of incident free-stream disturbances using large eddy simulations*. PhD thesis, University of Southampton, 2018.
- [3] WN Edeling, P. Cinnella, and R. Dwight. Predictive rans simulations via bayesian model-scenario averaging. *Journal of Computational Physics*, 275:65–91, 2014.
- [4] W. Edeling, M. Schmelzer, R. P Dwight, and P. Cinnella. Bayesian predictions of reynolds-averaged navier–stokes uncertainties using maximum a posteriori estimates. *AIAA Journal*, 56(5):2018–2029, 2018.

- 897 [5] R. Sandberg and V. Michelassi. The current state 932
898 of high-fidelity simulations for main gas path tur- 933
899 bomachinery components and their industrial im- 934
900 pact. *Flow, Turbulence and Combustion*, 102(2), 935
901 2019. 936
- 902 [6] K. Duraisamy, G. Iaccarino, and H. Xiao. Tur- 937
903 bulence modeling in the age of data. *Annual* 938
904 *Review of Fluid Mechanics*, 51, 2019. doi: 939
905 10.1146/annurev-fluid-010518-040547. 940
- 906 [7] X. Heng and P. Cinnella. Quantification of 941
907 model uncertainty in rans simulations: A review. 942
908 *Progress in Aerospace Sciences*, 108:1–31, 2019. 943
- 909 [8] B. Tracey, K. Duraisamy, and J.J. Alonso. Ap- 944
910 plication of supervised learning to quantify uncer- 945
911 tainties in turbulence and combustion modeling. 946
912 In *51st AIAA Aerospace Sciences Meeting*, 2013. 947
913 Dallas, TX, paper 2013-0259. 948
- 914 [9] E.J. Parish and K. Duraisamy. A paradigm for 949
915 data-driven predictive modeling using field inver- 950
916 sion and machine learning. *Journal of Computa-* 951
917 *tional Physics*, 305:758–774, 2016. 952
- 918 [10] J. Ling, A. Kurzwaski, and J. Templeton. 953
919 Reynolds averaged turbulence modelling using 954
920 deep neural networks with embedded invariance. 955
921 *Journal of Fluid Mechanics*, 807:155–166, 2016. 956
- 922 [11] J. Weatheritt and R. Sandberg. A novel evolution- 957
923 ary algorithm applied to algebraic modifications of 958
924 the RANS stress–strain relationship. *Journal of* 959
925 *Computational Physics*, 325:22–37, 2016. 960
- 926 [12] S.B. Pope. A more general effective-viscosity hy- 961
927 pothesis. *Journal of Fluid Mechanics*, 72:331— 962
928 340, 1975. 963
- 929 [13] H. Akolekar, R. Sandberg, N. Hutchins, 964
930 V. Michelassi, and G. Laskowski. Machine- 965
931 learnt turbulence closures for low pressure 966
turbines with unsteady inflow conditions. *Journal*
of Turbomachinery, 05 2019.
- [14] M. Schmelzer, R. P. Dwight, and P. Cinnella. Ma-
chine learning of algebraic stress models using de-
terministic symbolic regression, 2019.
- [15] S. Cheung, T. A. Oliver, E. E. Prudencio, and
R. Prudhomme, S. and D. Moser. Bayesian un-
certainty analysis with applications to turbulence
modeling. *Reliability Engineering & System*
Safety - RELIAB ENG SYST SAFETY, 96:1137–
1149, 09 2011.
- [16] Svetlana V Poroseva, M Yousuff Hussaini, and
Stephen L Woodruff. Improving the predictive ca-
pability of turbulence models using evidence the-
ory. *AIAA Journal*, 44(6):1220–1228, 2006.
- [17] P.D. Meyer, M. Ye, M. L. Rockhold, S. P Neu-
man, and K. J. Cantrell. Combined estimation of
hydrogeologic conceptual model, parameter, and
scenario uncertainty with application to uranium
transport at the hanford site 300 area. Technical
report, Pacific Northwest National Lab.(PNNL),
Richland, WA (United States), 2007.
- [18] Q Duan, N K Ajami, X Gao, and S Sorooshian.
Multi-model ensemble hydrologic prediction us-
ing Bayesian model averaging. *Advances in Water*
Resources, 30(5):1371–1386, 2007.
- [19] C Tebaldi and R Knutti. The use of the multi-
model ensemble in probabilistic climate projec-
tions. *Philosophical Transactions of the Royal*
Society of London A: Mathematical, Physical
and Engineering Sciences, 365(1857):2053–2075,
2007.
- [20] T Diomede, S Davolio, C Marsigli, MM Miglietta,
A Moscatello, P Papetti, T Paccagnella, A Buzzi,
and P Malguzzi. Discharge prediction based on

- 967 multi-model precipitation forecasts. *Meteorol-* 1002
968 *ogy and Atmospheric Physics*, 101(3-4):245–265, 1003
969 2008. 1004
- 970 [21] Rojas R., Kahunde S., Peeters L., Batelaan O., 1005
971 Feyen L., and Dassargues A. Application of a mul- 1006
972 timodel approach to account for conceptual model 1007
973 and scenario uncertainties in groundwater mod- 1008
974 elling. *Journal of Hydrology*, 394(3-4):416–435, 1009
975 2010. 1010
- 976 [22] D. Draper. Assessment and propagation of model 1011
977 uncertainty. *Journal of the Royal Statistical So-* 1012
978 *ciety: Series B (Methodological)*, 57(1):45–70, 1013
979 1995. 1014
- 980 [23] J A Hoeting, D Madigan, A E Raftery, and C T 1015
981 Volinsky. Bayesian model averaging: a tutorial. 1016
982 *Statistical science*, 14(4):382–401, 1999. 1017
- 983 [24] P. R. Spalart and S. R. Allmaras. One-equation tur- 1018
984 bulance model for aerodynamic flows. *Recherche* 1019
985 *aerospatiale*, (1):5–21, 1994. 1020
- 986 [25] David C Wilcox. *Turbulence modeling for CFD*. 1021
987 DCW Industries , La Canada, CA, 2006. 1022
- 988 [26] B. E. Launder and BI Sharma. Application of the 1023
989 energy-dissipation model of turbulence to the cal- 1024
990 culation of flow near a spinning disc. *Letters in* 1025
991 *heat and mass transfer*, 1(2):131–137, 1974. 1026
- 992 [27] X. Merle and P. Cinnella. Robust prediction of 1027
993 dense gas flows under uncertain thermodynamic 1028
994 models. *Reliability Engineering & System Safety*, 1029
995 183:400–421, 2019. 1030
- 996 [28] M. Arnst, R. Ghanem, and C. Soize. Identifica- 1031
997 tion of bayesian posteriors for coefficientsof chaos 1032
998 expansions. *Journal of Computational Physics*, 1033
999 229(9):3134–3154, 2010. 1034
- 1000 [29] W K. Hastings. Monte carlo sampling meth- 1035
1001 ods using markov chains and their applications. 1036
Biometrika, 57(1):97–109, 1970.
- [30] J. Geweke et al. *Evaluating the accuracy of sampling-based approaches to the calculation of posterior moments*, volume 196. Federal Reserve Bank of Minneapolis, Research Department Minneapolis, MN, 1991.
- [31] Leipold R., Boese M., and Fottner L. The influence of technical surface roughness caused by precision forging on the flow around a highly loaded compressor cascade. *Journal of turbomachinery*, 122(3):416–424, 2000.
- [32] L. Hilgenfeld and M. Pfitzner. Unsteady boundary layer development due to wake passing effects on a highly loaded linear compressor cascade. *Journal of Turbomachinery*, 126(4):493–500, 2004.
- [33] T. A Zaki, J.G Wissink, and P. A Rodi, W.and Durbin. Direct numerical simulations of transition in a compressor cascade: the influence of free-stream turbulence. *Journal of Fluid Mechanics*, 665:57–98, 2010.
- [34] Stephen B Pope. *Turbulent flows*, 2001.
- [35] S Tavoularis and U Karnik. Further experiments on the evolution of turbulent stresses and scales in uniformly sheared turbulence. *Journal of Fluid Mechanics*, 204:457–478, 1989.
- [36] L. Cambier, S. Heib, and S. Plot. The onera elsa cfd software: input from research and feedback from industry. *Mechanics & Industry*, 14(3):159–174, 2013.
- [37] F. Pedregosa, G. Varoquaux, A. Gramfort, V. Michel, B. Thirion, O. Grisel, M. Blondel, P. Prettenhofer, R. Weiss, V. Dubourg, J. Vanderplas, A. Passos, D. Cournapeau, M. Brucher, M. Perrot, and E. Duchesnay. Scikit-learn: Machine learning in Python. *Journal of Machine*

- 1037 *Learning Research*, 12:2825–2830, 2011.
- 1038 [38] C. Zhu, R.H Byrd, P. Lu, and J. Nocedal. Al-
1039 gorithm 778: L-bfgs-b: Fortran subroutines for
1040 large-scale bound-constrained optimization. *ACM*
1041 *Transactions on Mathematical Software (TOMS)*,
1042 23(4):550–560, 1997.
- 1043 [39] E. Jones, T. Oliphant, P. Peterson, et al. SciPy:
1044 Open source scientific tools for Python, 2001–.
- 1045 [40] V R. Joseph, E. Gul, and S. Ba. Maxi-
1046 mum projection designs for computer experi-
1047 ments. *Biometrika*, 102(2):371–380, 2015.
- 1048 [41] WN Edeling, Pasquale Cinnella, Richard P
1049 Dwight, and Hester Bijl. Bayesian estimates of
1050 parameter variability in the k - ε turbulence model.
1051 *Journal of Computational Physics*, 258:73–94,
1052 2014.